THE JOURNAL OF PHYSICAL CHEMISTRY C

Article

Cite This: J. Phys. Chem. C 2018, 122, 13944−13952

pubs.acs.org/JPCC

Dopant-Dependent SFG Response of Rhenium CO_2 Reduction Catalysts Chemisorbed on $SrTiO_3$ (100) Single Crystals

Aimin Ge,[†,§] Pablo E. Videla,[‡,§] Benjamin Rudshteyn,[‡] Qiliang Liu,[†] Victor S. Batista,*[,‡] and Tianquan Lian*[,†]

[†]Department of Chemistry, Emory University, 1515 Dickey Drive, NE, Atlanta, Georgia 30322, United States

[‡]Department of Chemistry and Energy Sciences Institute, Yale University, 225 Prospect Street, New Haven, Connecticut 06520, United States

Supporting Information

ABSTRACT: Monolayers of *fac*-Re(4,4′-dicarboxyl-2,2′-bipyridine)$(CO)_3Cl$ (ReC0A) complexes, covalently bound to TiO_2-terminated $SrTiO_3$ (100) (STO) single crystals, were studied by both vibrational Sum Frequency Generation (SFG) spectroscopy and Density Functional Theory (DFT). Homodyne-detected SFG results show that the SFG spectral shape of ReC0A on Nb-doped STO surfaces is almost opposite to that of ReC0A on undoped or Fe-doped STO surfaces, which we assign to a phase change of the SFG response of STO induced by the Nb rather than a change in orientation of the molecule. DFT calculations show that the doping with Nb populates the conduction band of the system, giving a metallic nature to the otherwise insulator STO substrate. This change in electronic structures of the substrate leads to a big nonresonant SFG response and thus interference with the spectra. The orientation of the ReC0A on all three substrates was found to be tilted by ∼45−50°, with a bidentate binding geometry and the Cl atom facing the surface. The reported results indicate that a molecular probe can be used to obtain information about the underlying material.

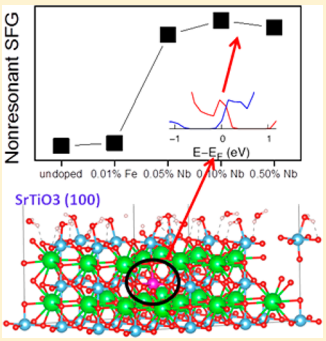

INTRODUCTION

Conversion of carbon dioxide (CO_2) into carbon-based fuels has been extensively studied as a potential approach for providing a renewable source of fuels with carbon neutral atmospheric footprint for the world's growing energy demands.[1,2] The rhenium (Re) tricarbonyl complex is one of the most extensively studied transition-metal complexes that show photo- and electrocatalytic activity for CO_2 reduction to CO.[3−9] Surface-immobilized Re catalyst systems have attracted increasing interest in recent years since they have the advantages of enhancing catalytic activity, reducing catalyst loading, and enabling convenient product separation.[10−13] In such heterogenized systems, the substrate plays a critical role in binding the catalysts and enabling charge and energy flow at the interface.[14] In this regard, it is essential to unravel the underlying substrate−adsorbate interactions to improve understanding of catalytic mechanism and develop molecular catalysts with higher catalytic efficiency and stability at electrode surfaces.

Re catalysts adsorbed on solid surfaces provide an opportunity to explore the effect of the surface electrode on the adsorbate by probing the C≡O stretching modes by vibrational spectroscopic techniques. Transient infrared spectroscopy has been used to study electron transfer between Re catalysts and TiO_2 thin films.[15,16] Two-dimensional infrared (2D-IR) spectroscopy has been used to study the adsorption structure, vibrational dynamics, and electron transfer of Re catalysts on surfaces.[17−20] In particular, vibrational sum frequency generation (SFG) has been employed to investigate the binding configurations of Re catalysts on semiconductor and metal surfaces.[21−24] Time-resolved SFG and two-dimensional SFG (2D-SFG) have been used to study ultrafast vibrational dynamics of Re catalysts on solid surfaces.[25−30] As an intrinsic surface-specific technique,[31,32] SFG shows great advantages over other vibrational spectroscopic techniques to probe catalyst monolayers adsorbed on flat metal surfaces and single-crystal semiconductor surfaces.

Previously, we have systematically explored binding motifs and vibrational dynamics of Re catalysts adsorbed on TiO_2 single crystals.[21−23,26] In the present work, we extended our studies to explore the *fac*-Re(4,4′-dicarboxyl-2,2′-bipyridine)-$(CO)_3Cl$ (ReC0A, Figure 1a) adsorbed on strontium titanate ($SrTiO_3$ or STO) (100) single crystals with different amounts of dopant elements. TiO_2-terminated STO surfaces prepared by wet etching provide a well-defined surface structure suitable for covalent attachment of ReC0A, which is useful for a detailed analysis of the molecular binding geometry. The doped STO single crystals also provide an opportunity to study electrocatalytic CO_2 reduction on oxide electrodes. In this work, both homodyne- and heterodyne-detected SFG together with density functional theory (DFT) are used to probe ReC0A/STO interfaces. We find that doping induces changes in the

Special Issue: Prashant V. Kamat Festschrift

Received: January 31, 2018
Revised: March 3, 2018
Published: March 5, 2018

DOI: 10.1021/acs.jpcc.8b01123
J. Phys. Chem. C 2018, 122, 13944−13952

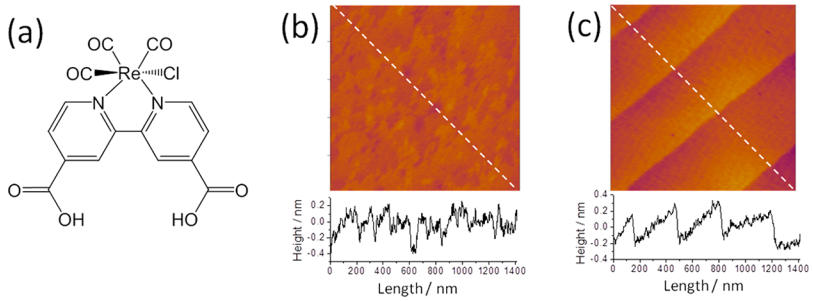

Figure 1. (a) Molecular structure of ReC0A. AFM images (1 μm × 1 μm) of (b) as-received and (c) etched undoped STO single crystal. The vertical profiles were taken along the white dash lines indicated in the images.

SFG response of ReC0A/STO, due to an increase in the nonresonance response. These result primarily from the substrate changes in metallic character more than from any significant changes in orientation of the adsorbate. To the best of our knowledge, this is the first characterization of the effect of doping on the SFG spectral response of molecular adsorbates.

■ EXPERIMENTAL SECTION

Sample Preparation. Undoped, 0.01 wt % Fe, 0.05 wt % Nb, 0.10 wt % Nb, and 0.50 wt % Nb doped $SrTiO_3$ (100) single crystals (10 × 10 × 0.5 mm or 10 × 5 × 0.5 mm, one side polished) were purchased from MTI Corporation. The surface of the as-received single crystals are composed of mixed SrO and TiO_2 layers as observed by atomic force microscopy (AFM) imaging (Figures 1b and S1). Atomically flat TiO_2-terminated STO surfaces were prepared by following the wet etching procedure reported by Kareev et al.[33] Briefly, the STO crystals were immersed in pure water to form a soluble hydroxide complex on the surface. Then, the surface SrO layer was removed by wet etching in HCl/HNO_3 (3:1) solution for 12 min. After that, the STO crystals were cleaned by ultrasonication in pure water and acetone followed by annealing at 1000 °C in air for 30 min (Carbolite, CWF 1100 °C chamber furnace). As shown in Figure 1c, the AFM image for the wet etched undoped STO shows a highly ordered surface structure. The vertical profile shows that the height of the terrace is ∼0.4 nm which corresponds to a single TiO_2 layer. It verifies the formation of atomically flat TiO_2-terminated STO surface.[34,35] TiO_2-terminated surfaces were also prepared for doped STO crystals (Figure S1). The TiO_2-terminated STO crystals were sensitized for 48 h in 1 mM ReC0A/ethanol solution, similar to the sample preparation of samples on TiO_2 single crystals.[21,23] After sensitization, the samples were rinsed by ethanol, dried by nitrogen stream, and stored in dark prior to use.

SFG Spectroscopic Measurements. The details of our femtosecond laser system have been described in previous papers.[23,24,36] The optical design for the heterodyne-detected SFG measurement is similar to the geometry as reported previously (Figure S2).[37,38] Briefly, a broad-band IR beam (wavelength center 5100 nm, full-width at half-maximum (fwhm) ∼ 200 cm^{-1}) and a narrow-band visible beam (800 nm, fwhm ∼ 10 cm^{-1}) are spatially and temporally overlapped on a bare gold thin film surface (used as the local oscillator). The incident angles of IR and visible beams with respect to this bare gold surface are 46° and 57°, respectively. The reflected IR, visible, and SFG beams were refocused on the sample surface by a concave mirror. The incident angles of IR and visible beams respect to the sample surface are 43° and 55°, respectively. A 2 or 3 mm thick CaF_2 plate was used to delay the SFG signal from the bare gold surface. The SFG signal generated from the sample surface was collinearly combined with the SFG signal from the bare gold surface (local oscillator, LO) to generate interferograms on the CCD detector. The reference spectrum was collected by replacing the sample with a bare gold thin film. The SFG signal generated from the LO was blocked to measure homodyne-detected SFG spectrum of sample on the second sample stage. *ppp* polarization combination (*p*-polarization for SFG, visible, and IR, respectively) was used for all measurements. Acquisition time for one SFG spectrum is typically 300 s. The data processing was performed with the Origin program. The phase of the complex spectra was corrected by using the A′(1) peak as a reference.[22,37] Details on the data processing method have been described in the literature.[22,37−39]

Computational Method. Model slabs of TiO_2-terminated $SrTiO_3$ (100) doped with Nb were obtained by DFT geometry relaxation, using the PBE exchange-correlation functional[40,41] and the projector augmented plane wave (PAW) method,[42,43] as implemented in the Vienna ab initio Simulation Package (VASP), version 5.3.5.[44−47] The PAW pseudopotentials include p-valence "Nb_pv" for Nb and s-valence "Sr_sv" for Sr. In general (VASP keyword in parentheses), the cutoff energy of plane wave basis was 600.0 eV ("ENMAX"), the Gaussian smear parameter was 0.1 eV ("SIGMA"), the energy convergence criterion was 10^{-4} eV per unit cell ("EDIFF"), the maximum optimization step size was 0.4 Bohr ("POTIM"), and the dispersion model used was Grimme's D3 correction with Becke-Johnson damping ("IVDW = 12").[48,49] The bulk calculation was based on a Monkhorst−Pack type k-point grid of 7 × 7 × 7.[50,51] The 6 × 6 × 5 nm slab (100) of TiO_2 was terminated with water adsorbed on top and was modeled with a 5 × 5 × 1 Monkhorst−Pack type k-point grid.[50,51] For all slab calculations, the bottom two layers were kept fixed to preserve the geometry of the crystal.

The bulk model of $SrTiO_3$ was validated by comparison to experimental lattice constants[52] and band gaps[53] as well as previous calculations,[54] as described in section 6 of the SI. The selection of the 5 × 5 × 1 k-point grid for analyzing DOS was validated by checking convergence, as described in section 7 of the SI.

For cluster calculations, the ωb97xd hybrid functional (which includes dispersion),[55] was used in conjunction with the LANL2DZ[56] basis set for the Ti, Re, and Sr atoms, and the 6-31G(d) basis set for the C, H, N, Cl, and O atoms,[37,38] as implemented in the Gaussian 09 suite of programs with other settings defined as by default.[57] Cluster models were carved out of the crystallographic slab, including nine $SrTiO_3$ units with

DOI: 10.1021/acs.jpcc.8b01123
J. Phys. Chem. C 2018, 122, 13944−13952

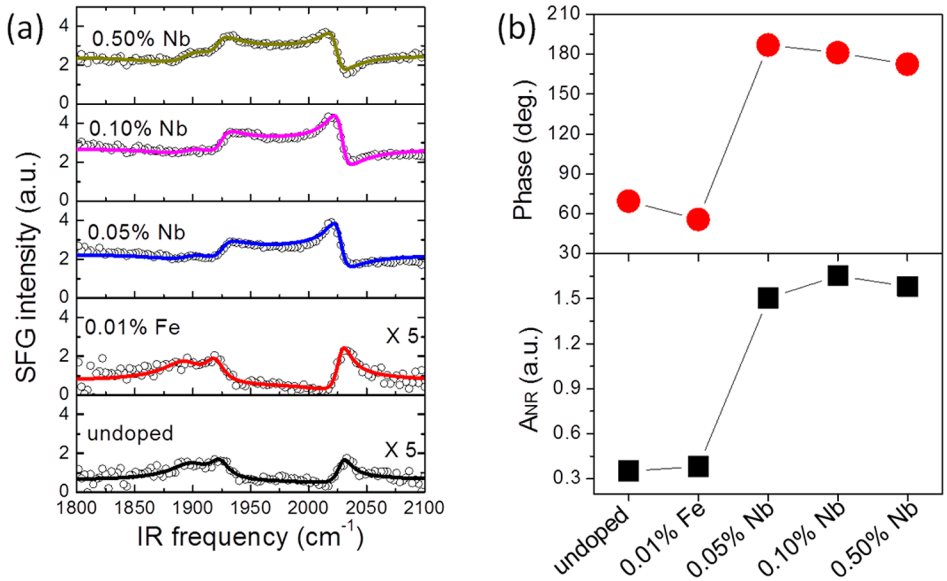

Figure 2. (a) Homodyne-detected SFG spectra for ReC0A adsorbed on TiO_2-terminated STO (100) surfaces. The spectra for ReC0A on undoped STO and 0.01 wt % Fe-doped STO are scaled by 5. Open circles are experimental data; solid curves are fits based on eq 1. (b) Fitted modulus and phase of the nonresonant signal. The errors based on spectral fits are shown in Table S1. Solid lines are provided to guide the eye.

terminating water and hydroxide groups accounting for the anionic charge on the carboxylates of the ReC0A catalyst bound through bidentate linkages. During the optimization process, only the ReC0A catalyst and the surface water molecules were allowed to relax.

We simulated the SFG spectra using frequencies and hyperpolarizabilities computed by DFT as in our previous work (additional details given in section 8 of the SI).[23,24,36] For these calculations, we used the B3LYP hybrid functional,[58−61] SDD for Re,[62] and the 6-311+G(d,p) basis set for the other atoms.[63,64] The "ultrafine" integration grid (99 radial shells and 590 angular points per shell) was used as implemented in the Gaussian 09 suite of programs.[57] Unless otherwise specified, the harmonic frequencies were scaled by 0.968.

■ RESULTS AND DISCUSSION

Influence of Doping on the SFG Responses. Figure 2a shows the homodyne-detected SFG spectra for ReC0A on TiO_2-terminated STO surfaces. For the ReC0A on undoped STO, the SFG spectrum is dominated by a narrow band around 2028 cm^{-1} and a broad band at the lower frequency region. The former band can be assigned to the in-phase symmetric C≡O stretching mode (A′(1)). The broad band are contributed from the antisymmetric mode (A″) at 1923 cm^{-1} and out-of-phase symmetric mode (A′(2)) at 1900 cm^{-1}, respectively.[22,23] The SFG spectrum of ReC0A on 0.01 wt % Fe-doped STO exhibits a similar line shape as that on undoped STO. On the other hand, for the Nb-doped STO substrates, the SFG spectra show two different features. First, the modulus of nonresonant SFG response from the Nb-doped STO is much stronger than either undoped or Fe-doped STO, as can be appreciated by considering the higher value of the baseline in Figure 2a. Second, the spectral shape is almost reversed in comparison with that of undoped or Fe-doped STO samples. Two possible explanations can be rationalized to explain the results. The first one involves a change in the up/down orientation of the molecule upon doping, modifying the molecular response and hence the SFG spectra. This change is unlikely since the self-assembly of carboxylate groups on atomically flat TiO_2 surfaces has been well characterized.[21,23] In addition, the lack of a spacer between the carboxylate group and the bipyridine ring for ReC0A excludes the possibility of a flip in orientation for the bipyridine ring. The second involves a change in the spectra due to interference between the resonant and nonresonant terms, akin to what is observed in gold substrates.[65,66]

To disentangle the reason for the spectral change upon doping, we fitted the experimental results. Usually, the vibrational SFG intensity can be expressed as[31,32]

$$I_{SFG} \propto \left| A_{NR} e^{i\phi_{NR}} + \sum_n \frac{A_n e^{i\phi_n}}{\omega_{IR} - \omega_n + i\Gamma_n} \right|^2 \quad (1)$$

where A_{NR} and ϕ_{NR} are the magnitude and phase of the nonresonant SFG response, respectively. A_n, ϕ_n, ω_n, and Γ_n are the amplitude, phase of amplitude, peak frequency, and damping constant of the nth vibrational mode. The fitting curves based on eq 1 are shown in Figure 2a, and the fitting parameters are listed in Table S1. The analysis of the obtained parameters shows that the resonant amplitudes A_n are reasonably constant for all the samples, suggesting that the orientation of the molecule is not significantly affected upon doping. In contrast, both the nonresonant magnitude A_{NR} and phase ϕ_{NR} change dramatically when comparing the undoped STO or Fe-doped STO to Nb-doped STO (Figure 2b). Hence, the reversed spectral shape observed for Nb-doped STO samples is attributed to a large phase change (∼120°) of the nonresonant SFG response (upper panel in Figure 2b).

The difference of nonresonant SFG responses is likely correlated to the different electronic properties of STO single crystals. The analysis of IR transmission spectra for all STO substrates (Figure S3a) shows that almost no IR light is transmitted through the 0.5 mm thick Nb-doped STO crystals, very different from undoped or Fe-doped STO crystals. Similarly, the UV−vis extinction spectra of STO substrates also show some differences (Figure S3b), although no significant differences are observed at 800 and 690 nm (the

DOI: 10.1021/acs.jpcc.8b01123
J. Phys. Chem. C 2018, 122, 13944−13952

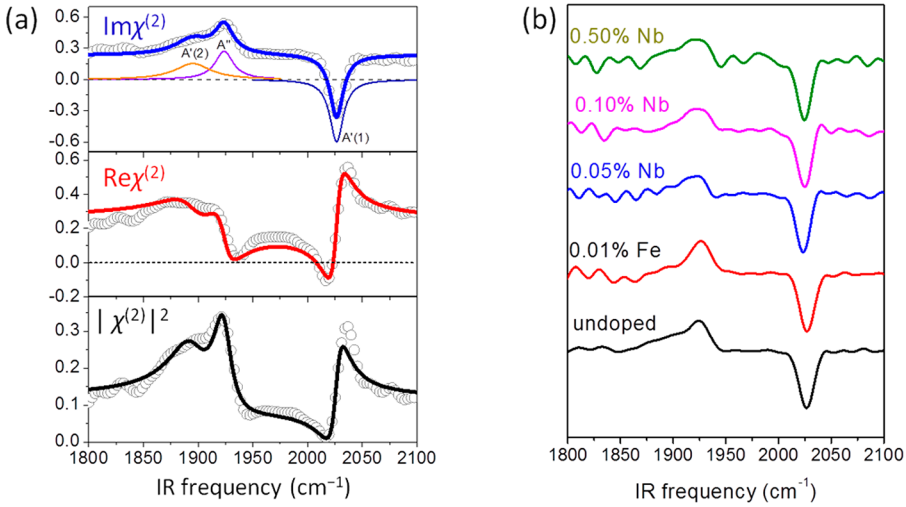

Figure 3. (a) Heterodyne-detected SFG spectra for ReC0A on TiO_2-terminated undoped STO surface. The $|\chi^{(2)}|^2$ spectrum is calculated from the imaginary and real components. Open circles are experimental data; solid lines are fitting results. The fitted imaginary spectra for individual vibrational mode are shown in the top panel. (b) Comparison of baseline-corrected imaginary spectra for ReC0A on different TiO_2-terminated STO surfaces. The intensity of the A′(1) mode is normalized. The spectra in (b) are arbitrarily offset for clarity.

wavelengths of the visible beam and of the SFG signal, respectively). These results are consistent with previous studies for STO, in which the Nb-doped STO was reported to have strong IR absorption around 2000 cm^{-1} possibly due to free carrier absorption.[67−69] In previous studies, it was reported that gold substrates show visible wavelength-dependent SFG response, which is directly correlated to the density of states and band structure of gold.[65,66] We conjecture that the different SFG responses of STO substrates are associated with the effect of doping on the electronic properties of STO. Such doping effects may also influence the interaction between semiconductor surfaces and adsorbates.

Heterodyne-Detected SFG Measurements. To remove the STO contribution from the SFG signal and improve the spectral analysis of the lower-frequency region, we performed heterodyne-detected SFG measurement for all samples. Unfortunately, the phase-corrected spectra cannot be used to determine the absolute up/down orientation of ReC0A since we had no precise control of the sample height or internal reference film deposited on the sample surface as reported in previous studies.[37−39] However, comparisons between the heterodyne-detected SFG spectra of different samples are still valid and allow us to discern changes in the orientation of the molecule upon substrate doping.

Figure 3a shows the imaginary and real parts as well as the $|\chi^{(2)}|^2$ spectra of ReC0A-undoped STO, respectively. One feature in the imaginary spectrum is that the sign of A′(1) mode is opposite to that of the A′′ and A′(2) modes. The simulated $|\chi^{(2)}|^2$ spectrum, which is based on the imaginary and real spectra, is consistent with the homodyne SFG spectrum as shown in Figure 2a. The heterodyne-detected SFG spectra for ReC0A on Fe-doped STO are found to be similar to those of Figure 3a. However, it was found that the heterodyne-detected SFG spectra of Nb-doped STO samples are always noisier than the other two samples with distorted baselines. It is possibly caused by the nonconstant intensity over the present spectral region for the Nb-doped resonance or the existence of multiple Nb-doped resonances, which are not fully considered in the simplified expression in eq 1. Figure 3b shows the baseline-corrected imaginary spectra of all samples. All spectra have similar features, suggesting that ReC0A molecules have similar orientations on all of these STO surfaces. Consistency in the orientation could be due to the low concentration of dopant (0.01 wt % ∼ 0.50 wt %) in both Fe and Nb-doped STO crystals. It is also noted that the peak intensity ratios between the two low-frequency C ≡ O modes (i.e., A′(2) and A′′) and the A′(1) mode are significantly larger than that of ReC0A on TiO_2 (001) and (110) single crystals, indicating different molecular orientations of ReC0A on TiO_2-terminated STO surface.[21,23]

Theoretical Assignment of Molecular Orientations. To examine the binding configuration of the ReC0A complex on the TiO_2-terminated STO surface, we perform DFT optimizations of the complex on a model $SrTiO_3$ cluster. Following our previous studies, where we found that the bidentate binding mode of the ReC0A complex on TiO_2 is energetically preferable,[21−23] we relaxed a bidentate binding motif on a small cluster model compose of nine $SrTiO_3$ units with terminal water molecules and hydroxide groups, as described in the Computational Method section.

To characterize the orientation of the complex on the surface, we make use of the Euler angles (Figure 4b) relating the molecular frame (Figure 4a) to the laboratory frame fixed on the surface according to the tilt (θ), twist (ψ), and rotation (φ) angles. Here, φ is the azimuthal angle describing the rotation of the molecule relative to the normal to the TiO_2 surface, while θ describes the tilt of the bipyridine plane relative to the normal. The angle ψ describes the rotation of the complex along the *c*-axis.

Two local energy minima were found for the bidentate binding motifs and are shown in Figure 4c,d. Both optimized structures present a tilted bipyridine ring with a tilt angle $\theta \sim 45°$, however, they differ in the twist angle. The first structure corresponds to a configuration with the Cl atom facing the surface (Figure 4c) and corresponds to the most energetically favorable configuration. The second structure is ∼7 kcal/mol higher in energy and corresponds to a configuration with the CO group facing the surface (Figure 4d), with a Cl group pointing away from the surface as in previous work.[23,24] Therefore, the structural modeling indicates that the ReC0A

DOI: 10.1021/acs.jpcc.8b01123
J. Phys. Chem. C 2018, 122, 13944−13952

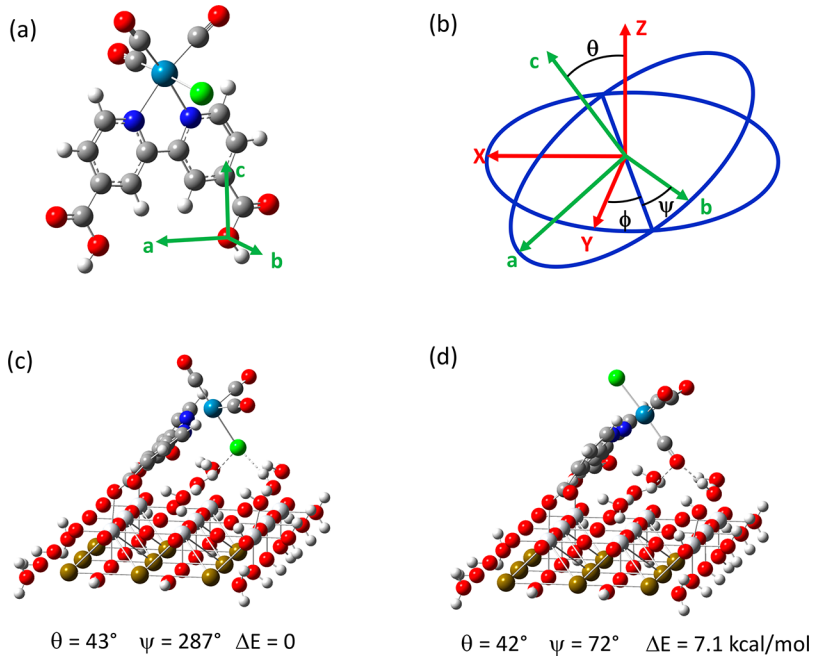

Figure 4. (a) Molecular axis system (*a*, *b*, *c*) of ReC0A complex. The *a*−*c* plane is defined as the plane of the bipyridine ring. (b) Schematic illustration of the Euler orientation angles used to characterize the orientation of the molecule on the STO surface. Axes *X*, *Y*, and *Z* represent the laboratory coordinates of the surface, while *a*, *b* and *c* represents the molecular coordinates of the complex. Orientation angles θ, ψ, and φ are the Euler transformation angles between the two Cartesian coordinates in the *ZYZ* rotation matrix formalism. (c, d) DFT optimized bidentate geometries of the molecule on STO surface. Values indicated are the tilt angle (θ), the twist angle (ψ), and the energy (ΔE) relative to the geometry labeled with "ΔE = 0". Color code: red = O, blue = N, white = H, gray = C, green = Cl, cyan = Re, silver = Ti, and dark orange = Sr.

complex binds in a bidentate tilted configuration with Cl facing the surface, likely unfavorable for CO_2 binding, as required for catalysis. Note that the minimum energy structure resembles the configuration previously found for the complex on the (110) facet of rutile TiO_2,[23] although with a greater tilt angle.

To further confirm the orientation found by DFT optimization, we computed the imaginary SFG spectra for each of the above motifs and compared them to the experimental data. The procedure to compute DFT-derived SFG spectra is based on previous studies[21−24,36] and is presented in the SI. Briefly, the calculations involve the determination of the second-order hyperpolarizability tensor $\beta^{(2)}_{ijk}$ at the DFT level and the subsequent rotation from the molecular to the laboratory frame (using Euler angles) to obtain the second-order susceptibility $\chi^{(2)}_{IJK}$. The final spectrum is related to the effective susceptibility that is a linear combination of different elements of the $\chi^{(2)}_{IJK}$ response and depends on both the Fresnel factors of the interface and the beam incident angles.

Typical spectra obtained for orientations close to the ones determined in the optimization are shown in Figure 5 (and Figure S6), exhibiting two positive peaks at low frequencies corresponding to the A′(2) and A″ stretching modes and one negative peak at higher frequency due to the symmetric A′(1) stretching mode. Computing the SFG spectra for a set of orientations close to the ones determined in the optimization, we found that the intensities of the modes are very sensitive to the orientation of the molecule. In particular, the relative intensity of the A′(2) and A″ stretching modes is highly dependent on small variations of the twist (ψ) angle (see Figure S6). Based on these results, we performed a scan on the tilt (θ) and twist (ψ) angles for orientations close to the configurations found in the DFT optimization (see section S8, SI). Following

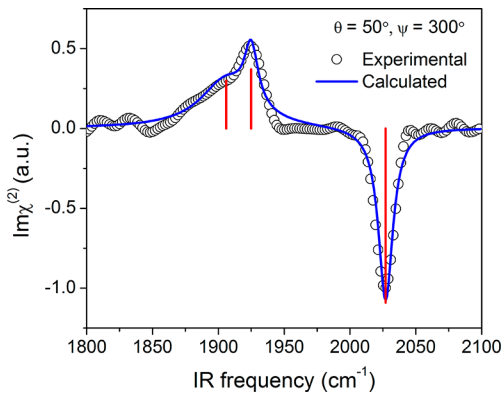

Figure 5. Best-matched DFT-based calculated imaginary SFG spectra (blue line) along with the experimental results (open circles) of ReC0A on undoped STO. Red lines indicate the frequency (ω) and amplitude (A/Γ) of each normal mode. The spectra correspond to a θ = 50°, ψ = 300° orientation.

previous studies,[24,36] frequencies and damping constant were allowed to relax within ±20 cm^{-1} and ±5 cm^{-1}, respectively, to obtain a more accurate spectral fit.

Figure 5 shows the best-matched calculated spectra along with the experimental result, showing excellent agreement between theory and experiments. The configuration giving rise to this spectrum corresponds to a θ = 50°, ψ = 300° orientation and is very close (within 10°) to the one found by the previous DFT optimization. Moreover, the frequencies and damping constant obtained from the fitting (Table S4) are in excellent agreement to those found by independently fitting to homodyne spectra (Table S1). The reported agreement supports the binding motif found by DFT optimization,

DOI: 10.1021/acs.jpcc.8b01123
J. Phys. Chem. C 2018, 122, 13944−13952

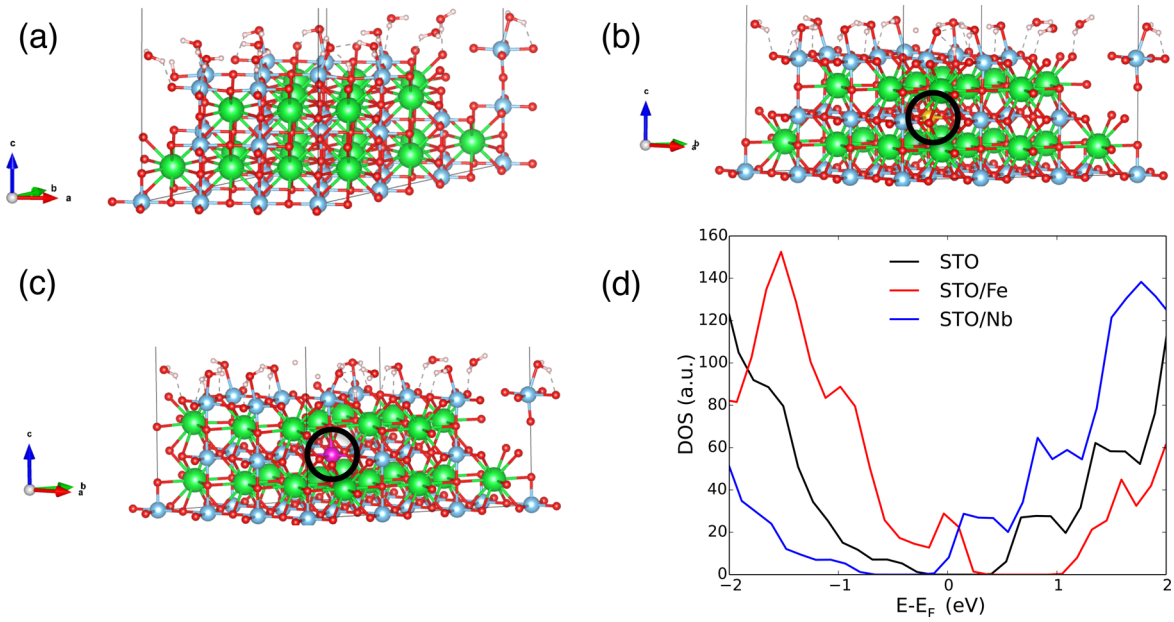

Figure 6. Geometries of the (a) no dopant (E_F = −1.58 eV), (b) Fe-doped (E_F = −2.18 eV), and (c) Nb-doped (E_F = −1.00 eV) slabs where the black circle points at the dopant as well as (d) the total density of states. Color code: red = O, bright green = Sr, blue = Ti, purple = Nb, and yellow = Fe.

demonstrating the value of DFT calculations for rigorous interpretation of SFG spectra.

For comparison, we performed calculations for binding structures with only one COOH group bound to the surface. Two local minimum energy structures were found for such a binding motif, similar to the bidentate bound configuration described above but exhibiting a more tilted and twisted orientation (Figure S7a,b). However, we ruled them out since the imaginary spectra obtained from these configurations disagree with experiments. In particular, for both monodentate structures, all the peaks in the spectra show the same positive sign, suggesting that these binding motifs are absent under the experimental conditions considered in this work.

Origin of the Dopant-Induced Nonresonant SFG Responses. From the previous analysis, it is clear that the differences encountered in the homodyne SFG spectra are due to a change in the nonresonant response of the surface and not due to a change of a molecular orientation. The kind of nonresonant response obtained for the Nb-doped samples is akin to the one found for gold substrate. In previous studies, it was reported that gold substrate shows visible wavelength-dependent SFG response, which is directly correlated to the density of states and band structure of gold.[65,66] Moreover, previous studies have found that doping the STO substrate with n-type dopants can alter the electronic properties of STO, giving metallic properties to the otherwise insulating STO system.[54,70,71] Hence, a change in electronic properties can explain the big difference between Nb-doped and undoped or Fe-doped samples.

In order to analyze the origin of the large nonresonant changes to the SFG upon Nb doping, we calculate the total density of states (DOS) for a slab model of the STO surface. The model consists of a 6 × 6 × 5 layer of a 100 facet TiO_2-terminated STO, passivated with water molecules (Figure 6a). For the doped-system case, we replace 1 Ti atom with the dopant atom (Figure 6b,c). Note that the formal concentration of the dopant in these calculations is $SrTi_{0.95}X_{0.05}O_3$ (X = Nb, Fe), much higher than the one used in the experiments, and hence, the computational results are only qualitative.

The DOS for the undoped system is presented as black lines in Figure 6d. The electronic structure is characterized by a band gap between the valence and conduction bands and, hence, the system behaves as an insulator. Projected DOS (PDOS) show that while the highest occupied molecular orbital in the valence band originates from O states, the lowest unoccupied molecular orbital in the conduction band is primary due to Ti states (Figure S8), in excellent agreement with previous studies.[54,70,71]

Upon incorporation of a Nb atom in the system, the Fermi level moves into the conduction band, giving metallic properties to the system (blue line). An analysis of the PDOS (Figure S9) reveals that the main contribution to the edge of the conduction band is due to Nb, Ti, and O states, with little contribution from the Sr states. Hence, Nb states are contributing more to the conducting band than the valence band, in accordance with previous studies.[54,70,71] In order to rationalize these findings in simple terms, it is instructive to realize that the Nb^{5+} ions occupy the Ti^{4+} sites in the lattice and hence act as n-type donor, populating the conduction band with electrons that act as free carriers.[52,54,70,71] This change in the electronic properties from insulator to metallic leads to a big nonresonant SFG response, along the lines of the nonresonance observed in gold substrates.[65,66]

■ CONCLUSION

We have shown that the rhenium bipyridyl catalyst ReC0A molecules chemisorbed on undoped and Nb/Fe-doped TiO_2-terminated $SrTiO_3$ (100) single crystals surfaces have similar binding geometries, as suggested by the combination of SFG spectroscopic measurements and DFT calculations. The Nb doping was found to affect the intensity and phase of the SFG response of STO substrate, likely due to the change in carrier density and thus metallic character of the substrate. The ReC0A was found to bind on the STO surface in bidentate motifs tilted at ∼45−50°, with the Cl atom facing the surface, which is

DOI: 10.1021/acs.jpcc.8b01123
J. Phys. Chem. C 2018, 122, 13944−13952

slightly different from ReC0A on TiO_2 (001) single crystals. The present work demonstrates that the Re catalyst monolayer with a well-defined structure can be assembled on conducting oxide single crystal surfaces and that the substrate's properties can be monitored using a molecular probe.

■ ASSOCIATED CONTENT

Supporting Information

The Supporting Information is available free of charge on the ACS Publications website at DOI: 10.1021/acs.jpcc.8b01123.

Additional AFM images, scheme of SFG setup, IR and UV−vis measurements, additional spectral fitting results, Fresnel factors, theoretical validation of models, description of theoretical SFG, and theoretical coordinates (PDF).

■ AUTHOR INFORMATION

Corresponding Authors

*E-mail: victor.batista@yale.edu.
*E-mail: tlian@emory.edu.

ORCID

Aimin Ge: 0000-0003-0127-3193
Benjamin Rudshteyn: 0000-0002-9511-6780
Victor S. Batista: 0000-0002-3262-1237
Tianquan Lian: 0000-0002-8351-3690

Author Contributions

[§]A.G. and P.E.V. made equal contributions.

Notes

The authors declare no competing financial interest.

■ ACKNOWLEDGMENTS

This work was supported by Air Force Office of Scientific Research Grants FA9550-17-0198. V.S.B. acknowledges computer time from the supercomputing facilities at Yale as well as at the Copper DoD HPCMP. A portion of the computational research was performed using EMSL (Ringgold ID 130367), a DOE Office of Science User Facility sponsored by the Office of Biological and Environmental Research. B.R. acknowledges support from the National Science Foundation Graduate Research Fellowship under Grant DGE-1122492. The authors thank Cliff Kubiak for helpful discussions.

■ REFERENCES

(1) Benson, E. E.; Kubiak, C. P.; Sathrum, A. J.; Smieja, J. M. Electrocatalytic and Homogeneous Approaches to Conversion of CO_2 to Liquid Fuels. *Chem. Soc. Rev.* **2009**, *38*, 89−99.

(2) White, J. L.; Baruch, M. F.; Pander, J. E., III; Hu, Y.; Fortmeyer, I. C.; Park, J. E.; Zhang, T.; Liao, K.; Gu, J.; Yan, Y.; et al. Light-Driven Heterogeneous Reduction of Carbon Dioxide: Photocatalysts and Photoelectrodes. *Chem. Rev.* **2015**, *115*, 12888−12935.

(3) Hawecker, J.; Lehn, J. M.; Ziessel, R. Electrocatalytic Reduction of Carbon Dioxide Mediated by Re(bipy)$(CO)_3$Cl (bipy = 2,2′-Bipyridine). *J. Chem. Soc., Chem. Commun.* **1984**, 328−330.

(4) Johnson, F. P.; George, M. W.; Hartl, F.; Turner, J. J. Electrocatalytic Reduction of CO_2 Using the Complexes [Re(bpy)$(CO)_3L]^n$ (n = +1, L= $P(OEt)_3$, CH_3CN; n= 0, L= Cl^-, Otf^-; bpy= 2, 2 '-Bipyridine; Otf^--= CF_3SO_3) as Catalyst Precursors: Infrared Spectroelectrochemical Investigation. *Organometallics* **1996**, *15*, 3374−3387.

(5) Smieja, J. M.; Kubiak, C. P. Re(bipy-tBu)$(CO)_3$Cl-improved Catalytic Activity for Reduction of Carbon Dioxide: IR-Spectroelectrochemical and Mechanistic Studies. *Inorg. Chem.* **2010**, *49*, 9283−9289.

(6) Sahara, G.; Ishitani, O. Efficient Photocatalysts for CO_2 Reduction. *Inorg. Chem.* **2015**, *54*, 5096−5104.

(7) Kumar, B.; Smieja, J. M.; Kubiak, C. P. Photoreduction of CO_2 on p-type Silicon Using Re(bipy-Bu^t)$(CO)_3$Cl: Photovoltages Exceeding 600 mV for the Selective Reduction of CO_2 to CO. *J. Phys. Chem. C* **2010**, *114*, 14220−14223.

(8) Sampson, M. D.; Froehlich, J. D.; Smieja, J. M.; Benson, E. E.; Sharp, I. D.; Kubiak, C. P. Direct Observation of the Reduction of Carbon Dioxide by Rhenium Bipyridine Catalysts. *Energy Environ. Sci.* **2013**, *6*, 3748−3755.

(9) Kuramochi, Y.; Ishitani, O.; Ishida, H. Reaction Mechanisms of Catalytic Photochemical CO_2 Reduction Using Re(I) and Ru(II) Complexes. *Coord. Chem. Rev.* **2017**, na DOI: 10.1016/j.ccr.2017.11.023.

(10) Windle, C. D.; Reisner, E. Heterogenised Molecular Catalysts for the Reduction of CO_2 to Fuels. *Chimia* **2015**, *69*, 435−441.

(11) Windle, C. D.; Pastor, E.; Reynal, A.; Whitwood, A. C.; Vaynzof, Y.; Durrant, J. R.; Perutz, R. N.; Reisner, E. Improving the Photocatalytic Reduction of CO_2 to CO Through Immobilisation of a Molecular Re Catalyst on TiO_2. *Chem. - Eur. J.* **2015**, *21*, 3746−3754.

(12) Oh, S.; Gallagher, J. R.; Miller, J. T.; Surendranath, Y. Graphite-Conjugated Rhenium Catalysts for Carbon Dioxide Reduction. *J. Am. Chem. Soc.* **2016**, *138*, 1820−1823.

(13) Schreier, M.; Luo, J.; Gao, P.; Moehl, T.; Mayer, M. T.; Grätzel, M. Covalent Immobilization of a Molecular Catalyst on Cu_2O Photocathodes for CO_2 Reduction. *J. Am. Chem. Soc.* **2016**, *138*, 1938−1946.

(14) Kraack, J. P.; Hamm, P. Surface-Sensitive and Surface-Specific Ultrafast Two-Dimensional Vibrational Spectroscopy. *Chem. Rev.* **2017**, *117*, 10623−10664.

(15) Asbury, J. B.; Hao, E.; Wang, Y. Q.; Ghosh, H. N.; Lian, T. Ultrafast Electron Transfer Dynamics From Molecular Adsorbates to Semiconductor Nanocrystalline Thin Films. *J. Phys. Chem. B* **2001**, *105*, 4545−4557.

(16) Abdellah, M.; El-Zohry, A. M.; Antila, L. J.; Windle, C. D.; Reisner, E.; Hammarström, L. Time-Resolved IR Spectroscopy Reveals a Mechanism with TiO_2 as a Reversible Electron Acceptor in a TiO_2−Re Catalyst CO_2 Photoreduction System. *J. Am. Chem. Soc.* **2017**, *139*, 1226−1232.

(17) Xiong, W.; Laaser, J. E.; Paoprasert, P.; Franking, R. A.; Hamers, R. J.; Gopalan, P.; Zanni, M. T. Transient 2D IR Spectroscopy of Charge Injection in Dye-Sensitized Nanocrystalline Thin Films. *J. Am. Chem. Soc.* **2009**, *131*, 18040−18041.

(18) Oudenhoven, T. A.; Joo, Y.; Laaser, J. E.; Gopalan, P.; Zanni, M. T. Dye Aggregation Identified by Vibrational Coupling Using 2D IR Spectroscopy. *J. Chem. Phys.* **2015**, *142*, 212449.

(19) Rosenfeld, D. E.; Gengeliczki, Z.; Smith, B. J.; Stack, T. D. P.; Fayer, M. D. Structural Dynamics of a Catalytic Monolayer Probed by Ultrafast 2D IR Vibrational Echoes. *Science* **2011**, *334*, 634−639.

(20) Kraack, J. P.; Frei, A.; Alberto, R.; Hamm, P. Ultrafast Vibrational Energy Transfer in Catalytic Monolayers at Solid-Liquid Interfaces. *J. Phys. Chem. Lett.* **2017**, *8*, 2489−2495.

(21) Anfuso, C. L.; Snoeberger, R. C., III; Ricks, A. M.; Liu, W.; Xiao, D.; Batista, V. S.; Lian, T. Covalent Attachment of a Rhenium Bipyridyl CO_2 Reduction Catalyst to Rutile TiO_2. *J. Am. Chem. Soc.* **2011**, *133*, 6922−6925.

(22) Anfuso, C. L.; Xiao, D.; Ricks, A. M.; Negre, C. F.; Batista, V. S.; Lian, T. Orientation of a Series of CO_2 Reduction Catalysts on Single Crystal TiO_2 Probed by Phase-Sensitive Vibrational Sum Frequency Generation Spectroscopy (PS-VSFG). *J. Phys. Chem. C* **2012**, *116*, 24107−24114.

(23) Ge, A.; Rudshteyn, B.; Psciuk, B. T.; Xiao, D.; Song, J.; Anfuso, C. L.; Ricks, A. M.; Batista, V. S.; Lian, T. Surface-Induced Anisotropic Binding of a Rhenium CO_2-Reduction Catalyst on Rutile TiO_2 (110) Surfaces. *J. Phys. Chem. C* **2016**, *120*, 20970−20977.

(24) Clark, M. L.; Rudshteyn, B.; Ge, A.; Chabolla, S. A.; Machan, C. W.; Psciuk, B. T.; Song, J.; Canzi, G.; Lian, T.; Batista, V. S.; et al. Orientation of Cyano-Substituted Bipyridine Re(I) *fac*-Tricarbonyl

DOI: 10.1021/acs.jpcc.8b01123
J. Phys. Chem. C 2018, 122, 13944−13952

Electrocatalysts Bound to Conducting Au Surfaces. *J. Phys. Chem. C* **2016**, *120*, 1657−1665.
(25) Anfuso, C. L.; Ricks, A. M.; Rodriguez-Cordoba, W.; Lian, T. Ultrafast Vibrational Relaxation Dynamics of a Rhenium Bipyridyl CO_2-Reduction Catalyst at a Au Electrode Surface Probed by Time-Resolved Vibrational Sum Frequency Generation Spectroscopy. *J. Phys. Chem. C* **2012**, *116*, 26377−26384.
(26) Ricks, A. M.; Anfuso, C. L.; Rodriguez-Cordoba, W.; Lian, T. Vibrational Relaxation Dynamics of Catalysts on TiO_2 Rutile (110) Single Crystal Surfaces and Anatase Nanoporous Thin Films. *Chem. Phys.* **2013**, *422*, 264−271.
(27) Wang, J.; Clark, M. L.; Li, Y.; Kaslan, C. L.; Kubiak, C. P.; Xiong, W. Short Range Catalyst-Surface Interactions Revealed by Heterodyne Two Dimensional Sum Frequency Generation Spectroscopy. *J. Phys. Chem. Lett.* **2015**, *6*, 4204−4209.
(28) Calabrese, C.; Vanselous, H.; Petersen, P. B. Deconstructing the Heterogeneity of Surface-bound Catalysts: Rutile Surface Structure Affects Molecular Properties. *J. Phys. Chem. C* **2016**, *120*, 1515−1522.
(29) Vanselous, H.; Stingel, A. M.; Petersen, P. B. Interferometric 2D Sum Frequency Generation Spectroscopy Reveals Structural Heterogeneity of Catalytic Monolayers on Transparent Materials. *J. Phys. Chem. Lett.* **2017**, *8*, 825−830.
(30) Ge, A.; Rudshteyn, B.; Zhu, J.; Maurer, R. J.; Batista, V. S.; Lian, T. Electron-Hole-Pair-Induced Vibrational Energy Relaxation of Rhenium Catalysts on Gold Surfaces. *J. Phys. Chem. Lett.* **2018**, *9*, 406−412.
(31) Shen, Y. Phase-Sensitive Sum-Frequency Spectroscopy. *Annu. Rev. Phys. Chem.* **2013**, *64*, 129−150.
(32) Wang, H. F.; Gan, W.; Lu, R.; Rao, Y.; Wu, B. H. Quantitative Spectral and Orientational Analysis in Surface Sum Frequency Generation Vibrational Spectroscopy (SFG-VS). *Int. Rev. Phys. Chem.* **2005**, *24*, 191−256.
(33) Kareev, M.; Prosandeev, S.; Liu, J.; Gan, C.; Kareev, A.; Freeland, J.; Xiao, M.; Chakhalian, J. Atomic Control and Characterization of Surface Defect States of TiO_2 Terminated $SrTiO_3$ Single Crystals. *Appl. Phys. Lett.* **2008**, *93*, 061909.
(34) Kawasaki, M.; Takahashi, K.; Maeda, T.; Tsuchiya, R. Atomic Control of the $SrTiO_3$ Crystal Surface. *Science* **1994**, *266*, 1540−1542.
(35) Koster, G.; Kropman, B. L.; Rijnders, G. J.; Blank, D. H.; Rogalla, H. Quasi-Ideal Strontium Titanate Crystal Surfaces Through Formation of Strontium Hydroxide. *Appl. Phys. Lett.* **1998**, *73*, 2920−2922.
(36) Ge, A.; Videla, P. E.; Lee, G. L.; Rudshteyn, B.; Song, J.; Kubiak, C. P.; Batista, V. S.; Lian, T. Interfacial Structure and Electric Field Probed by *in situ* Electrochemical Vibrational Stark Effect Spectroscopy and Computational Modeling. *J. Phys. Chem. C* **2017**, *121*, 18674−18682.
(37) Ge, A.; Peng, Q.; Qiao, L.; Yepuri, N. R.; Darwish, T. A.; Matsusaki, M.; Akashi, M.; Ye, S. Molecular Orientation of Organic Thin Films on Dielectric Solid Substrates: A Phase-Sensitive Vibrational SFG Study. *Phys. Chem. Chem. Phys.* **2015**, *17*, 18072−18078.
(38) Nihonyanagi, S.; Yamaguchi, S.; Tahara, T. Direct Evidence for Orientational Flip-Flop of Water Molecules at Charged Interfaces: A Heterodyne-Detected Vibrational Sum Frequency Generation Study. *J. Chem. Phys.* **2009**, *130*, 204704.
(39) Vanselous, H.; Petersen, P. B. Extending the Capabilities of Heterodyne-Detected Sum-Frequency Generation Spectroscopy: Probing Any Interface in Any Polarization Combination. *J. Phys. Chem. C* **2016**, *120*, 8175−8184.
(40) Perdew, J. P.; Burke, K.; Ernzerhof, M. Generalized Gradient Approximation Made Simple. *Phys. Rev. Lett.* **1996**, *77*, 3865−3868.
(41) Perdew, J. P.; Burke, K.; Ernzerhof, M. Generalized Gradient Approximation Made Simple [Phys. Rev. Lett. 77, 3865 (1996)]. *Phys. Rev. Lett.* **1997**, *78*, 1396−1396.
(42) Blöchl, P. E. Projector Augmented-Wave Method. *Phys. Rev. B: Condens. Matter Mater. Phys.* **1994**, *50*, 17953−17979.
(43) Kresse, G.; Joubert, D. From Ultrasoft Pseudopotentials to the Projector Augmented-Wave Method. *Phys. Rev. B: Condens. Matter Mater. Phys.* **1999**, *59*, 1758−1775.
(44) Kresse, G.; Furthmüller, J. Efficient Iterative Schemes for Ab Initio Total-Energy Calculations Using a Plane-Wave Basis Set. *Phys. Rev. B: Condens. Matter Mater. Phys.* **1996**, *54*, 11169−11186.
(45) Kresse, G.; Hafner, J. *Ab initio* Molecular Dynamics for Liquid Metals. *Phys. Rev. B: Condens. Matter Mater. Phys.* **1993**, *47*, 558−561.
(46) Kresse, G.; Hafner, J. *Ab initio* Molecular-Dynamics Simulation of the Liquid-Metal−Amorphous-Semiconductor Transition in Germanium. *Phys. Rev. B: Condens. Matter Mater. Phys.* **1994**, *49*, 14251−14269.
(47) Kresse, G.; Furthmüller, J. Efficiency of *ab initio* Total Energy Calculations for Metals and Semiconductors Using a Plane-Wave Basis Set. *Comput. Mater. Sci.* **1996**, *6*, 15−50.
(48) Grimme, S.; Antony, J.; Ehrlich, S.; Krieg, H. A Consistent and Accurate *ab initio* Parametrization of Density Functional Dispersion Correction (DFT-D) for the 94 Elements H-Pu. *J. Chem. Phys.* **2010**, *132*, 154104.
(49) Grimme, S.; Ehrlich, S.; Goerigk, L. Effect of the Damping Function in Dispersion Corrected Density Functional Theory. *J. Comput. Chem.* **2011**, *32*, 1456−1465.
(50) Monkhorst, H. J.; Pack, J. D. Special Points for Brillouin-Zone Integrations. *Phys. Rev. B* **1976**, *13*, 5188−5192.
(51) Pack, J. D.; Monkhorst, H. J. "Special Points for Brillouin-Zone Integrations"—A Reply. *Phys. Rev. B* **1977**, *16*, 1748−1749.
(52) Tomio, T.; Miki, H.; Tabata, H.; Kawai, T.; Kawai, S. Control of Electrical Conductivity in Laser Deposited $SrTiO_3$ Thin Films with Nb Doping. *J. Appl. Phys.* **1994**, *76*, 5886−5890.
(53) Cardona, M. Optical Properties and Band Structure of $SrTiO_3$ and $BaTiO_3$. *Phys. Rev.* **1965**, *140*, A651−A655.
(54) Guo, X. G.; Chen, X. S.; Sun, Y. L.; Sun, L. Z.; Zhou, X. H.; Lu, W. Electronic Band Structure of Nb Doped $SrTiO_3$ from First Principles Calculation. *Phys. Lett. A* **2003**, *317*, 501−506.
(55) Chai, J.-D.; Head-Gordon, M. Long-Range Corrected Hybrid Density Functionals with Damped Atom-Atom Dispersion Corrections. *Phys. Chem. Chem. Phys.* **2008**, *10*, 6615−6620.
(56) Hay, P. J.; Wadt, W. R. Ab Initio Effective Core Potentials for Molecular Calculations. Potentials for K to Au Including the Outermost Core Orbitals. *J. Chem. Phys.* **1985**, *82*, 299−310.
(57) Frisch, M. J.; Trucks, G. W.; Schlegel, H. B.; Scuseria, G. E.; Robb, M. A.; Cheeseman, J. R.; Scalmani, G.; Barone, V.; Mennucci, B.; Petersson, G. A. et al.. *Gaussian 09*, Revision D.01; Gaussian, Inc.: Wallingford, CT, 2013.
(58) Vosko, S. H.; Wilk, L.; Nusair, M. Accurate Spin-Dependent Electron Liquid Correlation Energies for Local Spin Density Calculations: A Critical Analysis. *Can. J. Phys.* **1980**, *58*, 1200−1211.
(59) Lee, C. T.; Yang, W. T.; Parr, R. G. Development of the Colle-Salvetti Correlation-Energy Formula into a Functional of the Electron Density. *Phys. Rev. B: Condens. Matter Mater. Phys.* **1988**, *37*, 785−789.
(60) Becke, A. D. Density-Functional Thermochemistry. III. The Role of Exact Exchange. *J. Chem. Phys.* **1993**, *98*, 5648−5652.
(61) Stephens, P. J.; Devlin, F. J.; Chabalowski, C. F.; Frisch, M. J. Ab Initio Calculation of Vibrational Absorption and Circular Dichroism Spectra Using Density Functional Force Fields. *J. Phys. Chem.* **1994**, *98*, 11623−11627.
(62) Andrae, D.; Haeussermann, U.; Dolg, M.; Stoll, H.; Preuss, H. Energy-Adjusted *ab initio* Pseudopotentials for the Second and Third Row Transition Elements. *Theor. Chim. Acta.* **1990**, *77*, 123−141.
(63) Krishnan, R.; Binkley, J. S.; Seeger, R.; Pople, J. A. Self-Consistent Molecular Orbital Methods. XX. A Basis Set for Correlated Wave Functions. *J. Chem. Phys.* **1980**, *72*, 650−654.
(64) McLean, A. D.; Chandler, G. S. Contracted Gaussian Basis Sets for Molecular Calculations. I. Second Row Atoms, Z = 11−18. *J. Chem. Phys.* **1980**, *72*, 5639−5648.
(65) Dreesen, L.; Humbert, C.; Celebi, M.; Lemaire, J.; Mani, A.; Thiry, P.; Peremans, A. Influence of the Metal Electronic Properties on the Sum-Frequency Generation Spectra of Dodecanethiol Self-

DOI: 10.1021/acs.jpcc.8b01123
J. Phys. Chem. C 2018, 122, 13944−13952

Assembled Monolayers on Pt (111), Ag (111) and Au (111) Single Crystals. *Appl. Phys. B: Lasers Opt.* **2002**, *74*, 621−625.
(66) Ishibashi, T.-a.; Onishi, H. A Multiplex Infrared-Visible Sum-Frequency Spectrometer With Wavelength Tunability of the Visible Probe. *Appl. Phys. Lett.* **2002**, *81*, 1338−1340.
(67) Maletic, S.; Maletic, D.; Petronijevic, I.; Dojcilovic, J.; Popovic, D. Dielectric and Infrared Properties of $SrTiO_3$ Single Crystal Doped by 3d (V, Mn, Fe, Ni) and 4f (Nd, Sm, Er) Ions. *Chin. Phys. B* **2014**, *23*, 026102.
(68) Baer, W. Free-Carrier Absorption in Reduced $SrTiO_3$. *Phys. Rev.* **1966**, *144*, 734−738.
(69) Gervais, F. o.; Servoin, J.-L.; Baratoff, A.; Bednorz, J. G.; Binnig, G. Temperature Dependence of Plasmons in Nb-Doped $SrTiO_3$. *Phys. Rev. B: Condens. Matter Mater. Phys.* **1993**, *47*, 8187−8194.
(70) Ozdogan, K.; Upadhyay Kahaly, M.; Sarath Kumar, S. R.; Alshareef, H. N.; Schwingenschlögl, U. Enhanced Carrier Density in Nb-Doped $SrTiO_3$ Thermoelectrics. *J. Appl. Phys.* **2012**, *111*, 054313.
(71) Baniecki, J.; Ishii, M.; Aso, H.; Kurihara, K.; Ricinschi, D. Density Functional Theory and Experimental Study of the Electronic Structure and Transport Properties of La, V, Nb, and Ta Doped $SrTiO_3$. *J. Appl. Phys.* **2013**, *113*, 013701.

DOI: 10.1021/acs.jpcc.8b01123
J. Phys. Chem. C 2018, 122, 13944−13952